Journal of Materials Chemistry C

PAPER

View Article Online
View Journal | View Issue

Cite this: J. Mater. Chem. C, 2018, 6, 3016

The electronic and optical properties of a narrow-band red-emitting nanophosphor $K_2NaGaF_6:Mn^{4+}$ for warm white light-emitting diodes†

Chunyan Jiang,[a] Mikhail G. Brik,[cde] Lihua Li,[a] Liyi Li,[a] Jie Peng,[a] Jianan Wu,[a] Maxim S. Molokeev,[fg] Ka-Leung Wong[h] and Mingying Peng*[ab]

Received 8th November 2017,
Accepted 21st February 2018

DOI: 10.1039/c7tc05098d

rsc.li/materials-c

Recently, as a key red component in the development of warm white light-emitting diodes (WLEDs), Mn^{4+}-doped fluorides with narrow red emission have sparked rapidly growing interest because they improve color rendition and enhance the visual energy efficiency. Herein, a red nanophosphor, $K_2NaGaF_6:Mn^{4+}$, with a diameter of 150–250 nm has been synthesized using a simple co-precipitation method. Rietveld refinement reveals that it crystallizes in the space group $Fm\bar{3}m$ with the cell parameter a = 8.25320(4) Å. The exchange charge model (ECM) has been used to calculate the energy levels of Mn^{4+} ions in K_2NaGaF_6, which match well with the experimental spectra. The as-synthesized phosphor exhibits a narrow red emission at around 630 nm (spin-forbidden $^2E_g \rightarrow {}^4A_2$ transition of Mn^{4+} ions) when excited at 365 nm ($^4A_{2g} \rightarrow {}^4T_{1g}$) and 467 nm ($^4A_{2g} \rightarrow {}^4T_{2g}$), with a quantum efficiency (QE) of 61% and good resistance to thermal quenching. Based on the structure, the formation mechanism of ZPL has been discussed. In addition, the concentration-dependent decay curves of Mn^{4+} in K_2NaGaF_6 were fitted using the Inokuti–Hirayama model, suggesting that the dipole–dipole interactions determine the concentration quenching. Finally, encouraged by the good performance, a warm LED with a CRI of 89.4 and CCT of 3779 K was fabricated by employing the title nanophosphor as the red component. Our findings suggest that $K_2NaGaF_6:Mn^{4+}$ can be a viable candidate for the red phosphor used in warm WLEDs.

1. Introduction

As is well-known, energy saving is one of the fundamental ways to ease the contradiction between development and energy shortage. The phosphor-converted white light-emitting diode (pc-WLED) has been recognized as an energy efficient technological solution because of its advantages of energy efficiency, robustness, long lifetime, and environmental friendliness.[1–6] Nowadays, the mainstream commercial pc-WLED is based on a blue chip and YAG:Ce^{3+} yellow phosphor. This combination provides the theoretical maximum conversion efficiency. However, the lack of red emission leads to the generation of cool white light with a low color rendering index (CRI, <80) and high correlated color temperature (CCT > 4500 K); this contradicts the new metric in the field of illumination-grade lighting focusing on high luminous and brilliant color rendering properties.[7] To compensate the red light deficiency in the emission spectrum, many efforts have been devoted to the development of red phosphors. Among them, Eu^{2+}-doped nitrides have been shown to be a class of promising red-emitting phosphors. They possess excellent luminescence properties and good thermal stability and chemical stability.[8–10] However, some drawbacks such as harsh synthesis conditions (usually high temperature, high pressure, and oxygen/water free), quantum loss resulting from re-absorption, and decreased energy efficiency due to insensitive deep red emission (>650 nm) still seriously hinder their wider commercialization. In this regard, how

[a] The China-Germany Research Center for Photonic Materials and Device, State Key Laboratory of Luminescent Materials and Devices, and Guangdong Provincial Key Laboratory of Fiber Laser Materials and Applied Techniques, School of Materials Science and Engineering, South China University of Technology, Guangzhou 510641, P. R. China. E-mail: pengmingying@scut.edu.cn
[b] School of Applied Physics and Materials, Wuyi University, Jiangmen, Guangdong 529020, P. R. China
[c] College of Mathematics and Physics, Chongqing University of Posts and Telecommunications, Chongqing 400065, P. R. China
[d] Institute of Physics, University of Tartu, W. Ostwald Str. 1, Tartu 50411, Estonia
[e] Institute of Physics, Jan Długosz University, Armii Krajowej 13/15, PL-42200 Częstochowa, Poland
[f] Laboratory of Crystal Physics, Kirensky Institute of Physics, Federal Research Center KSC SB RAS, Krasnoyarsk 660036, Russia
[g] Siberian Federal University, Krasnoyarsk 660041, Russia
[h] Department of Chemistry, Hong Kong Baptist University, Kowloon Tong, Hong Kong, P. R. China

† Electronic supplementary information (ESI) available: The crystallographic information file (CIF) of K_2NaGaF_6 is given. CCDC 433732. For crystallographic data in CIF see DOI: 10.1039/c7tc05098d

to further improve color rendition of pc-WLEDs without losing excess energy efficiency still remains a great challenge. One effective approach is to develop narrow-band red-emitting phosphors with emission spectrum adapted to the visual sensitivity of the human eye.[11,12]

Mn^{4+} ions have the $3d^3$ electron configuration and are usually stabilized at the octahedral sites. When doped in fluoride, Mn^{4+} exhibits a broad excitation located at 360 and 460 nm and a narrow emission band at 630 nm, which can well satisfy the abovementioned requirements (sensitive red emission and no reabsorption). In addition to superior optical luminescence properties, Mn^{4+}-doped fluorides are thermally stable and can be synthesized in a convenient way, thus attracting rapidly growing interest as red phosphors for white LEDs.[13] In 2014, Liu and Chen's group has reported a highly efficient red-emitting phosphor based on K_2TiF_6:Mn^{4+} that exhibits emission peaks at 608, 612, 630, 634, and 646 nm when excited at the maximum absorption peak at 460 nm.[14] By employing it as a red phosphor, a high performance white LED with a low correlated color temperature (3556 K), high color render index (CRI = 81), and luminous efficacy of 116 lm W^{-1} was fabricated. Immediately after this, many groups have reported the synthesis and performance of Mn^{4+}-doped fluoride red phosphors for warm WLEDs. Most studies have focused on A_2BF_6:Mn^{4+} (A = K^+, Na^+, Cs^+, Rb^+, and NH_4^+; B = Ge^{4+}, Ti^{4+}, Si^{4+}, Zr^{4+}, and Sn^{4+}) and $BaMF_6$:Mn^{4+} (M = Ge^{4+}, Ti^{4+}, and Si^{4+}).[15–21] Some of them with high luminous efficiency have promising applications in warm WLEDs;[15] some with low symmetry featuring strong ZPL emission have been proposed to further improve the CRI of WLEDs.[17] However, for most of them, Mn^{4+} was incorporated into the cationic sites with the same valence. Due to the similar ionic radius of Mn^{4+} and Al^{3+} (Ga^{3+}), it is strongly believed that Mn^{4+} can also be doped into the Al and Ga sites in fluoroaluminate and fluorogallate *via* non-equivalent substitution just like the case of Mn^{4+}-doped oxides ($Sr_4Al_{14}O_{25}$:Mn^{4+} and $Mg_3Ga_2GeO_8$:Mn^{4+}).[22,23] However, there are relatively few studies devoted to this approach.[24–26]

The elpasolite A_2BXF_6 (A = Na^+, K^+, Cs^+, Rb^+, B = Li^+, Na^+, K^+, X = Al^{3+}, Ga^{3+}) have various forms due to different cation combinations.[27] They possess stiff lattices with a band gap of >5 eV. When doped with rare earth ions, such as Ce^{3+} and Eu^{2+}, these materials emit in the UV region.[28] As this structure consists of isolated AlF_6 or GaF_6 octahedra, elpasolites are regarded as suitable hosts for Mn^{4+} doping. In this study, we report a red nanophosphor, K_2NaGaF_6:Mn^{4+}, synthesized using a simple co-precipitation method. The crystal structure, morphology, and composition of the samples were investigated in detail using XRD, Rietveld refinement, SEM, and TEM analyses. The luminescence properties including the diffuse reflection spectra, quantum yield, static and dynamic photoluminescence, concentration- and temperature-dependent spectra were studied systematically. Thereafter, as a proof of concept, the title phosphor was employed as a red component to fabricate a warm WLED, and the performance of the resulting LED under different drive currents was evaluated. The results show that K_2NaGaF_6:Mn^{4+} has a promising application potential in warm WLEDs.

2. Experimental and characterization

2.1 Materials

KF (99.99%), NaF (99.99%), $Ga(NO_3)_3$ (99.99%), HF (48 wt%), and KHF_2 (99.9%) were purchased from Aladdin Reagents. $KMnO_4$ (99.5%), acetone (AR), and H_2O_2 (30 wt%) were obtained from the Guangzhou Chemical Reagent Factory.

2.2 Preparation

The preparation of K_2MnF_6. The K_2MnF_6 precursor was prepared according to a literature procedure.[29] $KMnO_4$ (1.5 g) and KHF_2 (30 g) were weighed and dissolved in 100 mL of HF. After stirring for 30 min, the solution was placed in an ice bath. Then, 0.3 mL of H_2O_2 was added dropwise to the reaction mixture, the solution changed from purple to brown, and a yellow precipitate was obtained. The K_2MnF_6 precipitate was separated by centrifugation, washed several times using acetone, and then dried at 70 °C for 3 h.

The preparation of K_2NaGaF_6:Mn^{4+}. The K_2NaGaF_6:Mn^{4+} phosphor was prepared using a simple co-precipitation method. Taking K_2NaGaF_6:3% Mn^{4+} as an example, K_2MnF_6 (0.1483 g) was weighed and dissolved in 10 mL of HF, and after vigorous stirring for 5 min, $Ga(NO_3)_3$ (5.1148 g) was added. Thereafter, a solution of the salts of the remaining metals NaF (0.8389 g) and KF (2.3239 g) was added, and the mixed solution was stirred for further 20 min. Finally, the precipitate was separated by centrifugation, washed several times using acetone, and then dried at 70 °C for 3 h.

2.3 Characterization

The phase purity of the samples was checked by X-ray diffraction using a Bruker D8 ADVANCE X-ray diffractometer with Cu Kα radiation (λ = 0.15418 nm) at 40 kV and 40 mA. The powder diffraction data of K_2NaGaF_6 for Rietveld analysis was obtained at room temperature with the step size of $2\theta = 0.013^\circ$ and counting time = 1 s per step. The Rietveld refinement was performed using TOPAS 4.2.[30] High-resolution transmission electron microscopy (HRTEM) images were obtained using the JEOL JEM-2100 electron microscope operating at 200 kV. Scanning electron microscopy (SEM) images and the elemental composition were obtained using an FEI Nova NanoSEM403 scanning electron microscope equipped with an energy dispersive X-ray spectrometer (EDS) obtained from Bruker. The diffuse reflection spectra were obtained using a Cary 5000 UV-vis-NIR spectrophotometer equipped with a double out-of-plane Littrow monochromator using $BaSO_4$ powder as a standard reference. The static and dynamic spectra in the UV-visible range at room temperature were obtained using the Edinburgh FLS920 spectrometer equipped with a red-sensitive photomultiplier (Hamamatsu R928P), 450 W xenon lamp, and 60 W μF flash lamp with a pulse width of 1.5–3.0 μs and pulse repetition of 40 kHz. The absolute quantum yield was measured by a standard spectrometer (C11347-11, Hamamatsu Photonics K. K.). The temperature-dependent (25–300 °C) PL spectra were obtained using the Edinburgh FLS 920 spectrometer equipped with a homemade temperature controller. The color rendering index (CRI), luminous efficacy, correlated color temperature (CCT), as well as the

Commission International de l'Eclairage (CIE) chromaticity were evaluated by a photoelectricity test system (V2.00 LED spec system).

3. Calculation details

The electronic properties of the host were studied using the CASTEP module of Materials Studio.[31] The exchange–correlation functionals were represented by the generalized gradient approximation (GGA) and local density approximation (LDA).[32–34] The plane-wave basis energy cut-off was chosen at 410 eV, and ultrasoft pseudopotentials were used in all the calculations. The convergence parameters were as follows: total energy tolerance 5×10^{-6} eV per atom, maximum force tolerance 0.01 eV Å^{-1}, maximum stress component 0.02 GPa, and maximum displacement 5×10^{-4} Å. The *k*-points grid was chosen as $10 \times 10 \times 10$. The electronic configurations were $3s^2 3p^6 4s^1$ for K, $2s^2 2p^6 3s^1$ for Na, $3d^{10} 4s^2 4p^1$ for Ga, and $2s^2 2p^5$ for F.

As the next step to study the electronic and optical properties of the doped material, the exchange charge model (ECM) was used to calculate the energy levels of Mn^{4+} ions in K_2NaGaF_6.[35] All relevant details, including the equations used, their explanations, and calculation procedure, of the ECM have been described at length before (*e.g.*[35–37] and references therein); thus, they have not been repeated herein for brevity. Successful calculations of the energy level schemes of the transition metal and rare earth ions prove the reliability of the ECM. The crystal structure data of K_2NaGaF_6 were determined in the present study. After doping, Mn^{4+} ions occupy the Ga positions, which are 6-fold coordinated by fluorine ions. A cluster comprising 78 199 ions was used to calculate the crystal lattice sums.

4. Results and discussion

4.1 Crystal structure, morphology, and composition analysis

Rietveld refinement was carried out using the Topas 4.2 software to identify the phase and crystal structure of the as-prepared K_2NaGaF_6 compound. As all the peaks were well indexed by the cubic cell ($Fm\bar{3}m$) with parameters close to those of K_2NaCuF_6 (elpasolite-type structure),[38] the crystal structure of K_2NaCuF_6 was taken as the starting model for Rietveld refinement. Fig. 1a displays the Rietveld refinement pattern for K_2NaGaF_6. The experimental, calculated, and difference results of the XRD refinement of K_2NaGaF_6 are depicted using red, blue, and green lines, respectively. The goodness of the fit parameters R_{wp} = 6.12%, R_p = 4.54%, and R_B = 2.02% imply the phase purity of K_2NaGaF_6. The corresponding structural parameters obtained as a result of the refinement are shown in Table 1, and the crystallographic information file (CIF) is presented in the ESI.† The K_2NaGaF_6 compound crystallizes in a cubic structure with the space group $Fm\bar{3}m$. Its lattice parameter is fitted to be a = 8.25320(4) Å, and the unit cell volume V = 562.169(7) Å^3. The crystal structure of K_2NaGaF_6, as viewed along the *c*-axis, is shown in Fig. 1b; the compound is built up by co-vertex connected GaF_6 and NaF_6 octahedra with the K atoms occupying the 12-coordinated cavities.

Table 1 The refined structural parameters of the K_2NaGaF_6[a] sample

Atom	Site	*x*	*y*	*z*	occ	biso (Å^2)
K	8c	1/4	1/4	1/4	1	1.66(2)
Na	4b	1/2	1/2	1/2	1	1.22(3)
Ga	4a	0	0	0	1	0.77(2)
F	24e	0.2285(1)	0	0	1	1.76(2)

[a] Symmetry, cubic; space group, $Fm\bar{3}m$; a = 8.25320(4) Å, and V = 562.169(7) Å^3.

Fig. 2a presents the XRD patterns of $K_2NaGa_{1-x}F_6$:xMn^{4+} (x = 0.3%, 1.0%, 3.0%, 5.0%, and 7.0%). The simulated XRD pattern of the refined K_2NaGaF_6 is shown at the bottom as a reference. The XRD patterns of all the Mn^{4+}-doped K_2NaGaF_6 samples are similar and can be well indexed with the refined result of K_2NaGaF_6; this indicates that all the Mn^{4+}-doped K_2NaGaF_6 samples are of a pure phase. Moreover, the diffraction peaks shift slightly to the higher angle region with an increase in the Mn^{4+} concentration in $K_2NaGa_{1-x}F_6$:xMn^{4+}, as shown in Fig. 2b. This observation illustrates that Mn^{4+} has been successfully incorporated into the Ga^{3+} sites in K_2NaGaF_6 with a decrease in the inter-planar spacing d value as the radius of

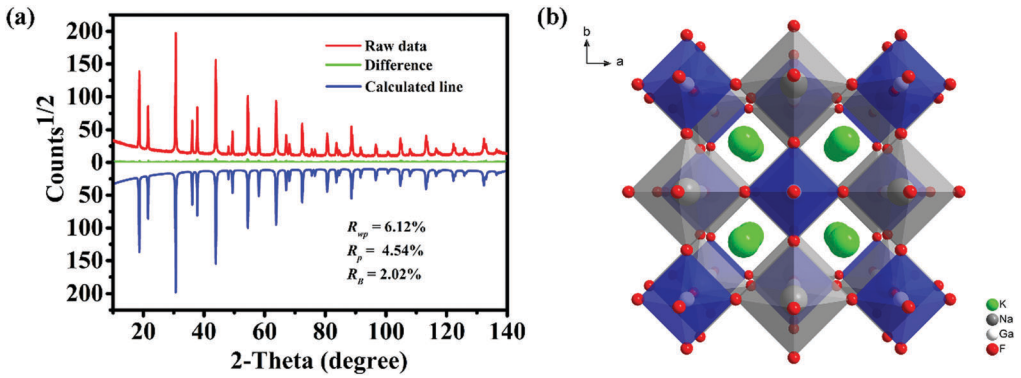

Fig. 1 (a) The experimental (red line) and calculated (blue line) XRD patterns and their difference (green line) for K_2NaGaF_6. (b) The structure of K_2NaGaF_6 viewed along the *c*-axis.

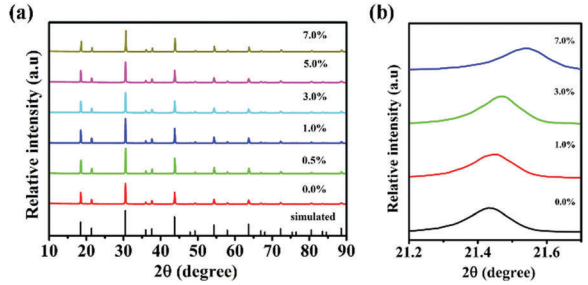

Fig. 2 (a) The XRD patterns of $K_2NaGa_{1-x}Mn_xF_6$ (x = 0, 0.5, 1.0, 3.0, 5.0, and 7.0%). (b) The peak shifts in the series of XRD patterns.

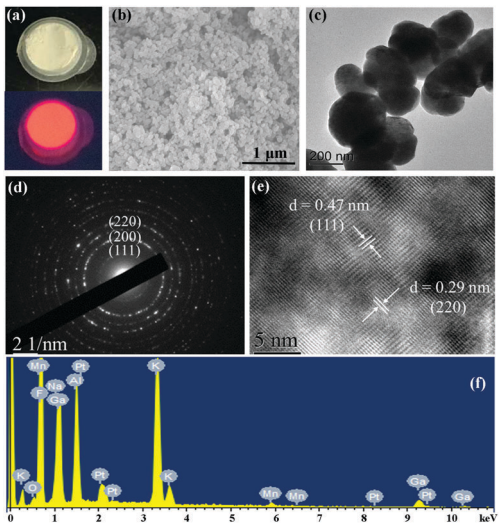

Fig. 3 (a) Images of the K_2NaGaF_6:3% Mn^{4+} sample obtained under a fluorescent lamp (upper image) and 365 nm UV lamp (lower image). (b) SEM image, (c) TEM image, (d) SAED pattern, (e) HRTEM image and (f) EDS analysis of the K_2NaGaF_6:3% Mn^{4+} sample.

Mn^{4+} (r = 0.52 Å, CN = 6) is smaller than that of Ga^{3+} (r = 0.62 Å, CN = 6).

The as-synthesized phosphor is a light yellow powder (Fig. 3a), and when exposed to 365 nm UV light, the phosphor emits intense red light. To further confirm the structure and morphology of K_2NaGaF_6:Mn^{4+}, HRTEM and SEM were employed. The SEM (Fig. 3b) and low-magnification TEM images (Fig. 3c) clearly show that the as-prepared K_2NaGaF_6:Mn^{4+} sample is sphere-like with diameter in the range of 150–250 nm. The EDS analysis results, as shown in Fig. 3f, demonstrate that the sample is composed of K, Na, Mn, Ga, and F. The weak Mn signal is attributed to its relatively low content, and the signals of Al and Pt originates from the aluminum support and conductive layer used in sample pretreatment steps. The atomic ratio (2 : 1 : 1 : 6) of K, Na, Ga, and F, as calculated from the EDS analysis, is in good agreement with the formula K_2NaGaF_6 and further illustrates the phase purity of the as-prepared sample. Fig. 3e displays the high resolution transmission electron microscopy (HRTEM) image; the lattice distances of 0.47 nm and 0.29 nm match well with the (111) and (220) crystal planes of K_2NaGaF_6, respectively. The legible lattice distance in the HRTEM image and typical SAED pattern (Fig. 3d) indicate good crystallization of the K_2NaGaF_6:Mn^{4+} samples.

4.2 Photoluminescence properties

4.2.1 Electronic structure and optical bandgap. The electronic properties of the host were studied using the CASTEP module of Materials Studio. The optimized lattice constants (8.4021 Å, GGA, and 8.0311 Å, LDA) are close to the corresponding experimental value of 8.2532 Å. The electronic band structure is shown in Fig. 4a. The band gap is direct, and the calculated band gaps of K_2NaGaF_6 are 5.925 eV (GGA) and 6.473 eV (LDA), respectively. These wide electronic band gaps favor doping with impurity ions (Mn^{4+} in particular) since this wide band gap ensures the location of the impurity energy levels in the host band gap. The origin of the electronic bands can be understood with the help of the density of states (DOS) diagrams shown in Fig. 4b. The conduction band (whose states exhibit well-pronounced dispersion) comprises the s and p states of K, Na, and Ga. The valence band stretches from about −5 eV to 0 and is dominated by the F 2p states. There are several narrow deep bands at −10 eV (K 3p and Ga 3d states), −20 eV (F 2s and Na 2p states), −26 eV (K 3s states), and −47 eV (Na 2s states).

To verify the band gap experimentally, the diffuse reflection spectra of the K_2NaGaF_6 host and K_2NaGaF_6:Mn^{4+} are depicted

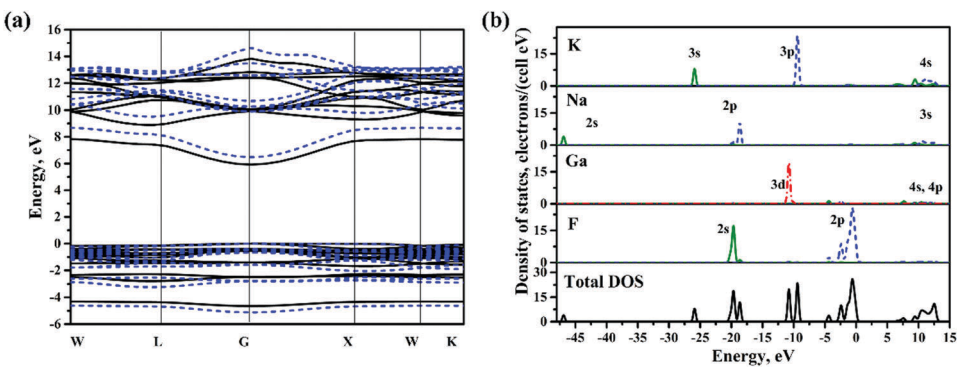

Fig. 4 (a) The calculated band structure (the solid line and dashed line present the results of GGA and LDA, respectively) obtained for K_2NaGaF_6. (b) The density of states (DOS) diagram obtained for K_2NaGaF_6 (the green solid line, blue dashed line, and red dashed line represent the s, p, and d states, respectively).

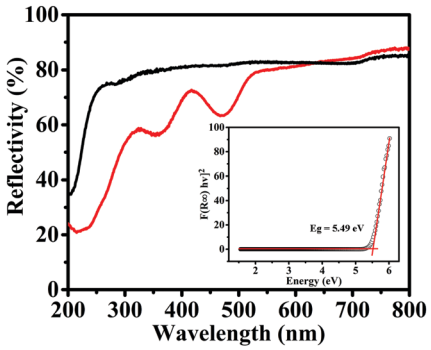

Fig. 5 The diffuse reflection spectra of the K_2NaGaF_6 host (black line) and K_2NaGaF_6:Mn^{4+} (red line) obtained at RT. The inset shows the plot of $[F(R_\infty)hv]^2$ *versus* energy (eV).

in Fig. 5. For the K_2NaGaF_6 host, the diffuse reflection spectrum shows a plateau of high reflection in the wavelength range of 250–800 nm, which then dramatically decreases from 250 to 200 nm. The absorption near 200 nm is attributed to the host absorption band. At first, to determine whether K_2NaGaF_6 is a direct band gap material or not, the plot of $[F(R_\infty)hv]^2$ *versus* $(hv - E_g)$ was determined, where hv is the photo energy,[39] E_g is the optical band gap energy, and $F(R_\infty)$ is the Kubelka–Munk function, defined as[40]

$$F(R_\infty) = (1 - R_\infty)^2/(2R_\infty) \quad (1)$$

where R_∞ denotes the reflectivity. The plot is shown in the inset of Fig. 5, and a linear dependence is observed, indicating that K_2NaGaF_6 is a direct band gap material, in agreement with our calculations. Then, by extrapolating the linear dependence to zero, the optical band gap of K_2NaGaF_6 was obtained as E_g = 5.49 eV, which agrees well with the calculated value of 5.925 eV (GGA) and is also comparable to that of other fluorides.[41,42] However, for Mn^{4+}-doped K_2NaGaF_6, the host absorption near 200 nm is red shifted; this might be due to the narrowed band gap after Mn^{4+} doping or overlapping of the charge transfer state of Mn^{4+}–F^- with host absorption.[17,43] Moreover, there are another two intense broad absorptions at 415–525 nm and 323–410 nm, whose origin has been discussed later. Notably, the strongest absorption is located in the blue region, which enables the phosphor to be a perfect match with a blue chip.

4.2.2 Crystal field calculations and spectroscopic data. The exchange charge model (ECM) was used to calculate the energy levels of Mn^{4+} ions in K_2NaGaF_6. K_2NaGaF_6 crystallizes in the $Fm\bar{3}m$ space group (No. 225) with the lattice constant a = 8.2532 Å. After doping, Mn^{4+} ions occupy the Ga^{3+} positions, which are 6-fold coordinated by fluorine ions at a distance of 1.8856 Å, forming an ideal octahedron. Due to the ideal octahedral symmetry, only two crystal field parameters are not zero. Their values (in cm^{-1}, Stevens normalization) are B_4^0 = 5598, B_4^4 = 27 990. The values of the Rach parameters B and C, which were chosen from the best agreement with experimental data, were B = 595 cm^{-1} and C = 3837 cm^{-1}. The calculated energy levels of Mn^{4+} ions in K_2NaGaF_6 are presented in Table 2, whereas Fig. 6a visualizes the good

Table 2 The calculated energy levels (in cm^{-1}) of Mn^{4+} ions in K_2NaGaF_6

Energy levels, O_h group notation	K_2NaGaF_6:Mn^{4+}
$^4A_{2g}$ (^4F)	0
^2E_g (^2G)	16 104
$^2T_{1g}$ (^2G)	16 539
$^4T_{2g}$ (^4F)	21 325
$^2T_{2g}$ (^2G)	24 522
$^4T_{1g}$ (^4F)	27 703
$^2A_{1g}$ (^2G)	35 216
$^2T_{2g}$ (^2H)	37 224
$^4T_{1g}$ (^4P)	45 196

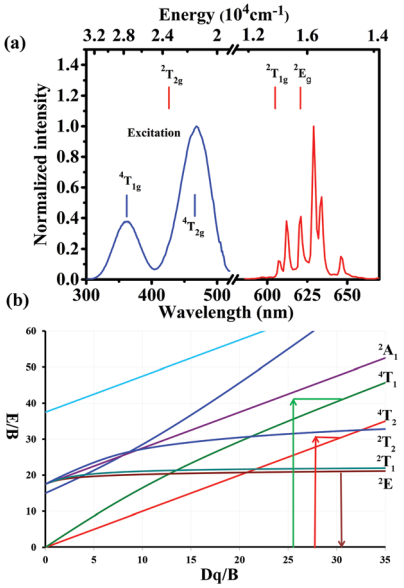

Fig. 6 (a) A comparison between the calculated energy levels of Mn^{4+} (vertical lines) and the experimental excitation/emission spectra (solid lines) of K_2NaGaF_6:Mn^{4+}. (b) The Tanabe–Sugano energy level diagram of Mn^{4+} in an octahedral crystal field.

agreement between the calculated energy levels and experimental excitation/emission spectra. In the photoluminescence excitation spectra, the two broad excitation bands centered at 365 nm and 467 nm in the range of 300–515 nm, with full width at half maxima of 47 nm and 53 nm, which are coincident with that shown in Fig. 5, are assigned to the spin-allowed $^4A_2 \rightarrow {}^4T_1$ and $^4A_2 \rightarrow {}^4T_2$ transitions (Fig. 6b), respectively. In the photo-luminescence emission spectra, there are several sharp lines in the range of 580–660 nm, originating from the $^2E \rightarrow {}^4A_2$ transition (Fig. 6b). For Mn^{4+}, the emission transition $^2E \rightarrow {}^4A_2$ is spin-forbidden, which usually couples with vibronic modes; hence, an emission spectrum featuring a zero-phonon line (ZPL) along with Stokes and anti-Stokes lines is obtained. The band at 621 nm is ascribed to the zero-phonon line (ZPL), the bands at 646, 634, and 629 nm are attributed to the Stokes lines, and the bands at 612, 606, and 598 nm are due to the anti-Stokes lines. The full width at half maximum of the emission band is 49 nm, which is considerably narrower than that of the commercial red phosphor $CaAlSiN_3$:Eu^{2+} (92 nm).[44] A distinct characteristic of the obtained emission spectra is the high intensity of the ZPL.

Referring to the relationship between the ZPL and symmetry, the symmetry of the Ga site was demonstrated to be O_h from the structural analysis, and there should be no ZPL. However, considering the unequal valence state and different ionic radius of Ga^{3+} and Mn^{4+}, the lattice can be partially distorted after doping. This partial site symmetry decrease caused by distortion may explain the strong ZPL observed in K_2NaGaF_6:Mn^{4+}, and a similar phenomenon takes place in other Mn^{4+}-doped high symmetry fluoroaluminates.[24,45]

4.2.3 Doping concentration-dependent luminescence. To check the relationship between the PL intensity and different doping concentrations, the emission spectra of $K_2NaGa_{1-x}F_6$:xMn^{4+} at different x values (x = 0.5%, 1%, 3%, 5%, and 7%) are depicted in Fig. 7a. Under excitation at 467 nm, the emission intensity of K_2NaGaF_6:Mn^{4+} initially increases with an increase in the doping concentration, reaches a maximum when the Mn^{4+} concentration is 3%, and then decreases upon further increasing the doping concentration (Fig. 7d). The critical concentration is 3% in this system. For comparison, Fig. 7b presents the normalized emission spectra of K_2NaGaF_6:Mn^{4+} at different doping concentrations. The contour of the spectra remains unchanged except the ZPL. The inset of Fig. 7b shows the change in the relative ZPL intensity. Upon increasing the Mn^{4+} concentration, the ZPL intensity increases as the lattice distortion becomes more serious due to more Mn^{4+} is doped into the larger Ga^{3+} sites. This fact further proves that the ZPL is derived from lattice distortion.

On the other hand, Fig. 7c presents the decay curves of the 621 nm emission of K_2NaGaF_6:Mn^{4+} upon excitation at 465 nm upon changing the Mn^{4+} concentration, and the lifetimes are shown in Fig. 7d. For a low concentration of Mn^{4+} (x = 0.5%), the decay curve is nearly a single exponential, and the emission intensity y after t s decay can be written as

$$y = y_0 \exp\left[-\left(\frac{t}{\tau}\right)\right] \quad (2)$$

where τ is the intrinsic lifetime, y_0 presents the initial intensity, and t is the time. The intrinsic lifetimes of Mn^{4+} (x = 0.5%, 1.0%) were fitted to be 5.68 ms, which is similar to that of Mn^{4+} in another host.[46] While for a higher concentration of Mn^{4+} (x = 1.0%, 3.0%, 5.0%, and 7.0%), the decay curves gradually deviate from a single exponential, and the lifetimes are shortened; this indicates that an extra decay channel is active. That is the Mn^{4+}–Mn^{4+} energy transfer becomes more efficient upon increasing the Mn^{4+} concentration. The excitation energy migrates over and depletes in a quenching center. The lifetime shortens as a result of non-radiative energy migration.[47] To hypothesize the nature of the interaction process under the critical concentration, the Inokuti–Hirayama model was introduced to investigate the shape of the decay curves for different multi-polar interactions.[48]

$$I(t) = I(0)\exp\left[-\left(\frac{t}{\tau}\right) - \frac{4\pi}{3}\Gamma\left(1-\frac{3}{s}\right)C_A C_{DA}{}^{3/s} t^{3/s}\right] \quad (3)$$

where $I(0)$ is the initial emission intensity, t is the time after excitation, τ is the intrinsic lifetime of Mn^{4+}, $\Gamma()$ is a gamma function, C_A is the concentration of Mn^{4+}, C_{DA} is the energy transfer micro-parameter, and s stands for the specific multi-polar interaction: 6, 8, and 10 for the dipole–dipole, dipole–quadrupole, and quadrupole–quadrupole interactions, respectively. When s is set to 6, the best fitting could be achieved, as shown in Fig. 7c, suggesting that dipole–dipole was the main interaction in the energy transfer process. According to the fitting results, the average C_{DA} is 5.5946×10^{-45} m^6 s^{-1}.

For luminescence, the quantum yield is an important parameter for a phosphor and determines its performance directly. The inner quantum yield is defined by[49]

$$\eta_{in} = \frac{\int L_S}{\int E_R - \int E_S} \quad (4)$$

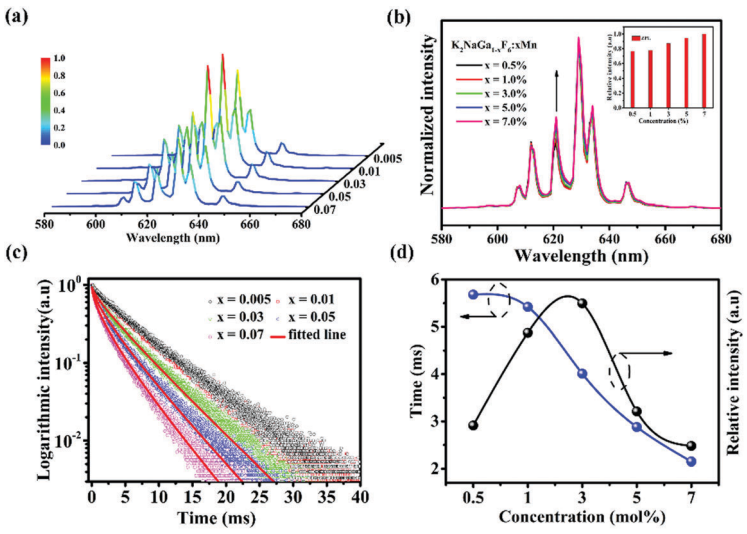

Fig. 7 (a) The emission spectra (under excitation at 467 nm) and (b) normalized emission spectra obtained for K_2NaGaF_6:xMn^{4+} (x = 0.5%, 1%, 3%, 5%, and 7%). The inset shows the relative ZPL intensity of K_2NaGaF_6:Mn^{4+} as a function of the doping concentration. (c) The decay curves of the 621 nm emission (under excitation at 467 nm) observed for $K_2NaGa_{1-x}F_6$:xMn^{4+} (x = 0.5%, 1%, 3%, 5%, and 7%). (d) The lifetime and relative integrated intensity of K_2NaGaF_6:Mn^{4+} as a function of the doping concentration.

where L_S is the emission intensity of the sample, and E_S and E_R are the spectra of the excitation light with and without the sample in the integrating sphere, respectively. All the spectra were obtained using Hamamatsu Photonics. Based on the abovementioned equation, the inner quantum yield of the optimum concentration sample $K_2NaGa_{0.97}F_6$:3%Mn^{4+} under excitation at 467 nm is calculated to be 61%.

4.3 Thermal stability

For a phosphor, thermal stability is another essential aspect while evaluating the performance of an LED because it changes the color coordinates and lowers the luminous efficiency.[50] Fig. 8a shows the temperature-dependent emission spectra of the optimum concentration sample $K_2NaGa_{0.97}F_6$:3%Mn^{4+} under excitation at 467 nm. Obviously, the emission intensity drops continuously with an increase in temperature, and the relative intensities at different temperatures are shown in Fig. 8b. When the temperature reaches 150 °C, the emission intensity drops to 71.9% of the initial PL intensity. To further investigate the dynamics of the Mn^{4+} luminescence process, the emission spectra were normalized to the highest intensity, as shown in Fig. 8c. With an increase in temperature, the relative ZPL intensity decreases, whereas the anti-Stokes intensity increases. This means that the ZPL emission competes with the anti-Stokes emission in the radiative process.[17] As the temperature increases, the excited electron tends to populate the higher vibration levels. Hence, the anti-Stokes emission with an emission energy higher than that of the ZPL transition is more likely to happen than the ZPL emission. On the other hand, the decay curves of the 621 nm emission in $K_2NaGa_{0.97}F_6$:3%Mn^{4+} at different temperatures were also investigated and are depicted in Fig. 8d. The decay occurs faster upon increasing the temperature. The lifetime drops from 5.60 ms to 2.78 ms from 25 °C to 200 °C (Fig. 8b). The decrease in both the lifetime and luminescence illustrate thermal quenching in $K_2NaGa_{0.97}F_6$:3%Mn^{4+}. The probability of thermal quenching is strongly related to the activation energy, systematic studies have shown that the emission intensity decreases exponentially with the activation energy, and their relationship can be expressed as follows:[51]

$$\frac{I(T)}{I_0} = \left[1 + A\exp\left(-\frac{\Delta E}{k_B T}\right)\right]^{-1} \quad (5)$$

where I_0 is the initial emission intensity, $I(T)$ is the intensity at temperature T, ΔE is the activation energy, A is a constant, and k_B is the Boltzmann's constant. ΔE is fitted to be 0.324 eV, which is relatively high when compared with that of other Mn^{4+}-doped phosphors.[52,53]

In addition to the thermal quenching behavior, the chromaticity stability was also studied. Fig. 8f presents the changes in the CIE chromaticity coordinates of $K_2NaGa_{0.97}F_6$:3%Mn^{4+} at different temperatures. The chromaticity coordinates shift from (0.6901, 0.3098) to (0.6806, 0.3192) as the temperature is increased from room temperature to 200 °C. Furthermore, to quantify the variations, the chromaticity shifts (ΔE) were calculated based on the following equation:

$$\Delta E = \sqrt{(u_t' - u_0')^2 + (v_t' - v_0')^2 + (w_t' - w_0')^2} \quad (6)$$

where $u' = 4x/(3 - 2x + 12y)$, $v' = 9y/(3 - 2x + 12y)$, $w' = 1 - u' - v'$. u', v', and w' are the chromaticity coordinates in uniform color space 1976, and x and y are the chromaticity coordinates in CIE 1931. u_t' and u_0' represent the chromaticity coordinates u at 25 °C and a given high temperature, respectively. The calculated CIE shifts of $K_2NaGa_{0.97}F_6$:3%Mn^{4+} in the temperature range from 50 °C to 200 °C are plotted in Fig. 8e. The chromaticity shift is 10.8×10^{-3} at 150 °C and 22.0×10^{-3} at 200 °C. By contrast, the chromaticity shift of $CaAlSiN_3$:Eu^{2+} is 25.6×10^{-3} at 150 °C and 39.2×10^{-3} at 200 °C.[54] This result indicates that the chromaticity stability in K_2NaGaF_6:Mn^{4+} is superior to that of the commercial red phosphor $CaAlSiN_3$:Eu^{2+}.

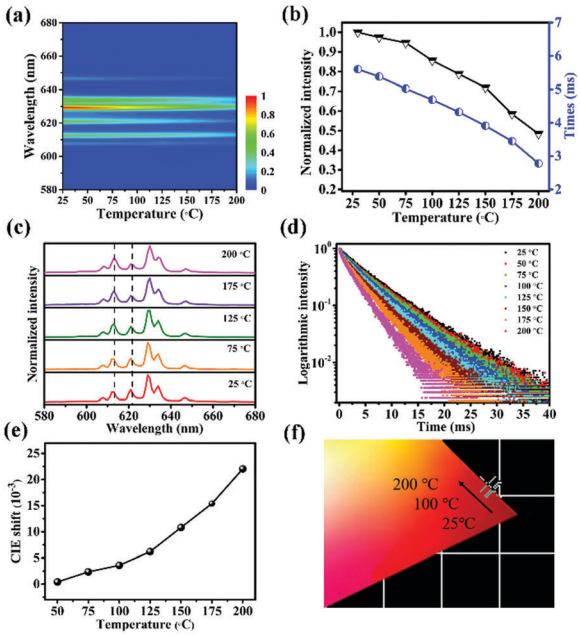

Fig. 8 (a) The emission spectra of $K_2NaGa_{0.97}F_6$:3%Mn^{4+} under excitation at 467 nm, (b) the integrated emission intensity and lifetime of $K_2NaGa_{0.97}F_6$:3%Mn^{4+}, (c) the highest height-normalized emission spectra of $K_2NaGa_{0.97}F_6$:3%Mn^{4+}, (d) the decay curves of the 626 nm emission of $K_2NaGa_{1-x}F_6$:3%Mn^{4+} under excitation at 467 nm and (e) the chromaticity shift and (f) CIE chromaticity coordinates of $K_2NaGa_{1-x}F_6$:3%Mn^{4+} at different temperatures.

4.4 Application in WLEDs

Due to the appropriate optical properties, the potential application of the as-prepared phosphor in WLEDs was further evaluated. A series of LEDs (LED I-LED III) was fabricated using the method of blue chip + commercial yellow phosphor($Y_3Al_5O_{12}$:Ce^{3+}) + different amounts of the title red phosphor (K_2NaGaF_6:3%Mn^{4+}). The blue chip used herein is a chip-on-board type with a wavelength of 450–460 nm and power of 200 mW. Fig. 9a–c present the electroluminescence spectra of the as-fabricated LEDs and their corresponding images at a drive current of 20 mA. It is obvious that the red region increases markedly upon increasing the content of K_2NaGaF_6:3%Mn^{4+}. The color coordinates of the LEDs move

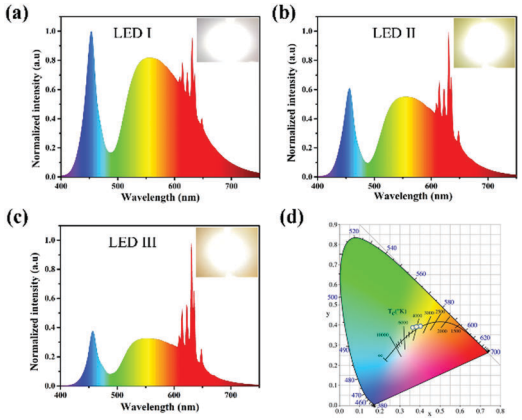

Fig. 9 (a–c) The electroluminescence (EL) spectra and (d) CIE chromaticity diagram of the WLEDs fabricated with different K_2NaGaF_6/YAG:Ce^{3+} ratios under a 20 mA drive current.

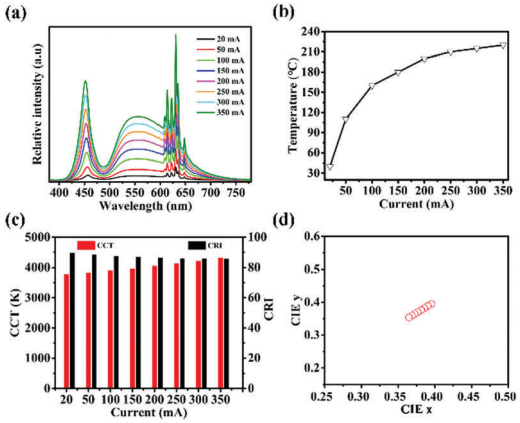

Fig. 10 (a) The electroluminescence (EL) spectra, (b) junction temperature, (c) correlated color temperature, color rendering index and (d) color coordinates of LED III under different drive currents.

Table 3 The chromaticity coordinates and performance parameters of the fabricated WLEDs

No.	YAG : KNGF (weight ratio)	Current (mA)	CCT (K)	CRI	Chromaticity coordinate		Luminous efficiency (lm W^{-1})
					x	y	
I	1 : 5	20	4496	75.9	0.3640	0.3812	110.59
II	1 : 7	20	4132	80.0	0.3785	0.3911	94.32
III	1 : 9	20	3779	89.4	0.3967	0.3937	84.37

gradually to the warm white region in the CIE 1931 color spaces, as shown in Fig. 9d. Table 3 shows the performance test of the LED devices, and due to the addition of the red phosphor K_2NaGaF_6:3%Mn^{4+}, the color rendering index of the LED is effectively improved from 75.9, 80 to 89.4, and the color temperature changes from 4496 K, 4132 K to 3779 K. For the optimum LED III, the CIE color coordinate lies near the black body locus, and the luminous efficiency is 84.37 lm W^{-1}. The corresponding devices emit bright warm light, as shown in the inset of Fig. 9c. Due to the excellent performance of the blue chip and phosphors, the luminous efficacy of the as-prepared WLED is superior to that of the white-light up-conversion.[55] These inspiring results indicate that the red phosphor K_2NaGaF_6:Mn^{4+} may potentially be used in warm WLEDs.

Furthermore, the effect of the drive current on the performance of LED III was investigated. Fig. 10a presents the electroluminescence spectra of LED III under different drive currents. As can be seen, the emission intensity enhances gradually upon increasing the drive current, and no saturation phenomenon is detected. In addition, the shape of the emission spectra changes little with the drive current; thus, LED III undergoes slight color temperature, CRI, and color coordinate shifts, as seen in Fig. 10c and d. When the drive current increases from 20 to 350 mA, the color temperature increases from 3779 K to 4304 K, whereas the CRI decreases from 89.4 to 85.5. More importantly, the practical junction temperature of the LED was also measured and exhibited in Fig. 10b. It provides information that for a high power LED device, the junction temperature usually exceeds 50 °C, and it increases upon increasing the drive current. When the drive current is 350 mA, the junction temperature can even reach 210 °C. However, the emission intensity increases continuously. This means that the thermal stability of the phosphor is appropriate, and no obvious thermal quenching is observed.

5. Conclusions

In summary, a novel red nanophosphor, K_2NaGaF_6:Mn^{4+}, has been synthesized using a simple co-precipitate method. The phase purity was confirmed by XRD and Rietveld refinement. The SEM and TEM analyses reveal that the phosphor is 150–250 nm in diameter with high crystallinity. The energy levels of Mn^{4+} ions in K_2NaGaF_6 were calculated using the ECM method of crystal field theory and allowed the assignment of spectra. The K_2NaGaF_6:Mn^{4+} phosphor exhibits a narrow red luminescence at around 630 nm when excited at 467 nm with a quantum yield of 61%. The ZPL appears due to the partial lattice distortion that occurs after doping. For K_2NaGaF_6:Mn^{4+}, the optimum concentration was determined to be 3%. Efficient energy transfer dominated by dipole–dipole interactions is proposed to be responsible for the concentration quenching effect. Moreover, the phosphor exhibits relatively good thermal stability, and the integrated emission intensity of K_2NaGaF_6:3%Mn^{4+} drops to 71.9% of its initial emission intensity at 150 °C. Finally, as a proof of concept, a warm WLED with a CRI of 89.4, color temperature of 3779 K, and luminous efficiency of 84.37 lm W^{-1} was fabricated. The fabricated WLED exhibits slight color temperature and CRI change with an increase in the drive current from 20 to 350 mA. The present study demonstrates that K_2NaGaF_6:Mn^{4+} can be a promising red phosphor in warm WLEDs.

Conflicts of interest

There are no conflicts to declare.

Acknowledgements

We acknowledge the financial support received from the Program for Innovative Research Team in University of Ministry of Education of China (Grant No. IRT_17R38), the Key Program of Guangzhou Scientific Research Special Project (Grant No. 201607020009), the National Natural Science Foundation of China (Grant No. 51672085, 51322208, 3160440), and the Fundamental Research Funds for the Central Universities. M. G. Brik acknowledges the supports received from the Recruitment Program of High-end Foreign Experts (Grant No. GDW20145200225), the Programme for the Foreign Experts offered by Chongqing University of Posts and Telecommunications, Ministry of Education and Research of Estonia, (Project PUT430) and European Regional Development Fund (Project TK141), and the Guest Professorship at Kyoto University (Prof. S. Tanabe laboratory). The first-principles calculations were carried out using the resources provided by the Wroclaw centre for Networking and Supercomputing (http://wcss.pl; Grant No. WCSS#10117290).

References

1 T. Justel, H. Nikol and C. Ronda, *Angew. Chem., Int. Ed.*, 1998, **37**, 3085.
2 E. F. Schubert and J. K. Kim, *Science*, 2005, **308**, 1274.
3 S. Pimputkar, J. S. Speck, S. P. DenBaars and S. Nakamura, *Nat. Photonics*, 2009, **3**, 179.
4 G. X. Bai, M. K. Tsang and J. H. Hao, *Adv. Funct. Mater.*, 2016, **26**, 6330.
5 L. Chen, C. C. Lin, C. W. Yeh and R. S. Liu, *Materials*, 2010, **3**, 2172.
6 L. Chen, K. J. Chen, C. C. Lin, C. I. Chu, S. F. Hu, M. H. Lee and R. S. Liu, *J. Comb. Chem.*, 2010, **12**, 587.
7 P. Pust, P. J. Schmidt and W. Schnick, *Nat. Mater.*, 2005, **18**, 13.
8 P. Pust, V. Weiler, C. Hecht, A. Tuecks, A. S. Wochnik, A. K. Henss, D. Wiechert, C. Scheu, P. J. Schmidt and W. Schnick, *Nat. Mater.*, 2014, **13**, 891.
9 R. J. Xie and N. Hirosaki, *Sci. Technol. Adv. Mater.*, 2007, **8**, 588.
10 C. W. Yeh, W. T. Chen, R. S. Liu, S. F. Hu, H. S. Sheu, J. M. Chen and H. T. Hintzen, *J. Am. Chem. Soc.*, 2012, **134**, 14108.
11 C. C. Lin, A. Meijerink and R. S. Liu, *J. Phys. Chem. Lett.*, 2016, **7**, 495.
12 J. H. Oh, Y. J. Eo, H. C. Yoon, Y. D. Huh and Y. R. Do, *J. Mater. Chem. C*, 2016, **4**, 8326.
13 H. D. Nguyen and R. S. Liu, *J. Mater. Chem. C*, 2016, **4**, 10759.
14 H. M. Zhu, C. C. Lin, W. Q. Luo, S. T. Shu, Z. G. Liu, Y. S. Liu, J. T. Kong, E. Ma, Y. G. Cao, R. S. Liu and X. Y. Chen, *Nat. Commun.*, 2014, **5**, 4312.
15 J. H. Oh, H. Kang, Y. J. Eo, H. K. Park and Y. R. Do, *J. Mater. Chem. C*, 2015, **3**, 607.
16 M. H. Fang, H. D. Nguyen, C. C. Lin and R. S. Liu, *J. Mater. Chem. C*, 2015, **3**, 7277.
17 W. L. Wu, M. H. Fang, W. L. Zhou, T. Lesniewski, S. Mahlik, M. Grinberg, M. G. Brik, H. S. Sheu, B. M. Cheng, J. Wang and R. S. Liu, *Chem. Mater.*, 2017, **29**, 935.
18 H. D. Nguyen, C. C. Lin, M. H. Fang and R. S. Liu, *J. Mater. Chem. C*, 2014, **2**, 10268.
19 X. Y. Jiang, Z. Chen, S. M. Huang, J. G. Wang and Y. X. Pan, *Dalton Trans.*, 2014, **43**, 9414.
20 Q. Zhou, Y. Y. Zhou, Y. Liu, L. J. Luo, Z. L. Wang, J. H. Peng, J. Yan and M. M. Wu, *J. Mater. Chem. C*, 2015, **3**, 3055.
21 X. Y. Jiang, Y. X. Pan, S. M. Huang, X. A. Chen, J. G. Wang and G. K. Liu, *J. Mater. Chem. C*, 2014, **2**, 2301.
22 M. Y. Peng, X. W. Yin, P. A. Tanner, M. G. Brik and P. F. Li, *Chem. Mater.*, 2015, **27**, 2938.
23 X. Ding, G. Zhu, W. Y. Geng, Q. Wang and Y. H. Wang, *Inorg. Chem.*, 2016, **55**, 154.
24 Y. W. Zhu, L. Huang, R. Zou, J. H. Zhang, J. B. Yu, M. M. Wu, J. Wang and Q. Su, *J. Mater. Chem. C*, 2016, **4**, 5690.
25 E. H. Song, J. Q. Wang, J. H. Shi, T. T. Deng, S. Ye, M. Y. Peng, J. Wang, L. Wondraczek and Q. Y. Zhang, *ACS Appl. Mater. Interfaces*, 2017, **9**, 8805.
26 T. T. Deng, E. H. Song, J. Sun, L. Y. Wang, Y. Deng, S. Ye, J. Wang and Q. Y. Zhang, *J. Mater. Chem. C*, 2017, **5**, 2910.
27 I. N. Flerov, M. V. Gorev, J. Grannec and A. Tressaud, *J. Fluorine Chem.*, 2002, **116**, 9.
28 P. D. Belsare, S. V. Moharil, C. P. Joshi and S. K. Omanwar, *AIP Conf. Proc.*, 2011, **1391**, 194.
29 H. Bode, H. Jenssen and F. Bandte, *Angew. Chem.*, 1953, **65**, 304.
30 P. Jacobs, A. Houben, W. Schweika, A. L. Tchougreeff and R. Dronskowski, *J. Appl. Crystallogr.*, 2015, **48**, 1627.
31 S. J. Clark, M. D. Segall, C. J. Pickard, P. J. Hasnip, M. J. Probert, K. Refson and M. C. Payne, *Z. Kristallogr.*, 2005, **220**, 567.
32 J. P. Perdew, K. Burke and M. Ernzerhof, *Phys. Rev. Lett.*, 1996, **77**, 3865.
33 D. M. Ceperley and B. J. Alder, *Phys. Rev. Lett.*, 1980, **45**, 566.
34 J. P. Perdew and A. Zunger, *Phys. Rev. B: Condens. Matter Mater. Phys.*, 1981, **23**, 5048.
35 N. M. Avram and M. G. Brik, *Optical properties of 3d-ions in crystals*, Springer and Tsinghua University Press, 2013, vol. 8, p. 63.
36 M. G. Brik and A. M. Srivastava, *Opt. Mater.*, 2016, **54**, 245.
37 B. Z. Malkin, N. M. Abishev, E. I. Baibekov, D. S. Pytalev, K. N. Boldyrev, M. N. Popova and M. Bettinelli, *Phys. Rev. B*, 2017, **96**, 014116.
38 S. Schneider and R. Hoppe, *Z. Anorg. Allg. Chem.*, 1970, **376**, 268.
39 X. Ding and Y. Wang, *ACS Appl. Mater. Interfaces*, 2017, **9**, 23983.
40 H. N. James, *Rev. Prog. Color. Relat. Top.*, 1985, **15**, 66.
41 T. Takahashi and S. Adachi, *J. Electrochem. Soc.*, 2008, **155**, E183.
42 P. Rawat, S. K. Saroj, M. Gupta, G. V. Prakash and R. Nagarajan, *J. Fluorine Chem.*, 2017, **200**, 1.

43 B. Venugopal, B. Nandan, A. Ayyachamy, V. Balaji, S. Amirthapandian, B. K. Panigrahi and T. Paramasivam, *RSC Adv.*, 2014, **4**, 6141.
44 Z. Wang, B. Shen, F. Dong, S. Wang and W. S. Su, *Phys. Chem. Chem. Phys.*, 2015, **17**, 15065.
45 Y. W. Zhu, L. Y. Cao, M. G. Brik, X. J. Zhang, L. Huang, T. T. Xuan and J. Wang, *J. Mater. Chem. C*, 2017, **5**, 6420.
46 L. Q. Xi, Y. X. Pan, M. M. Zhu, H. Z. Lian and J. Lin, *J. Mater. Chem. C*, 2017, **5**, 9255.
47 S. S. Liang, M. M. Shang, H. Lian, K. Li, Y. Zhang and J. Lin, *J. Mater. Chem. C*, 2017, **5**, 2927.
48 M. Inokuti and F. Hirayama, *J. Chem. Phys.*, 1965, **43**, 1978.
49 H. Chen, H. Lin, Q. Huang, F. Huang, J. Xu, B. Wang, Z. Lin, J. Zhou and Y. Wang, *J. Mater. Chem. C*, 2016, **4**, 2374.
50 L. P. Wang, N. J. Long, L. H. Li, Y. Lu, M. Li, J. K. Cao, Y. Zhang, Q. Y. Zhang, S. H. Xu, Z. M. Yang, C. B. Mao and M. Y. Peng, *Light: Sci. Appl.*, 2018, **7**, DOI: 10.1038/s41377-018-0007-z.
51 C. W. Struck and W. H. Fonger, *J. Appl. Phys.*, 1971, **42**, 4515.
52 M. M. Zhu, Y. X. Pan, L. Q. Xi, H. Z. Lian and J. Lin, *J. Mater. Chem. C*, 2017, **5**, 10241.
53 T. Hu, H. Lin, Y. Cheng, Q. M. Huang, J. Xu, Y. Gao, J. M. Wang and Y. S. Wang, *J. Mater. Chem. C*, 2017, **5**, 10241.
54 X. J. Zhang, Y. T. Tsai, S. M. Wu, Y. C. Lin, J. F. Lee, H. S. Sheu, B. M. Cheng and R. S. Liu, *ACS Appl. Mater. Interfaces*, 2016, **8**, 19612.
55 J. Wang, J. H. Hao and P. A. Tanner, *Opt. Lett.*, 2010, **35**, 3922.